Journal of Molecular Structure 1239 (2021) 130455

Contents lists available at ScienceDirect

Journal of Molecular Structure

journal homepage: www.elsevier.com/locate/molstr

# Pseudotetrahedral high-spin manganese(II)-complexes with (*S* or *R*)-N-1-(Ar)ethyl-salicylaldimine: Chiroptical property, chirality induction at-metal, paramagnetism, redox-potential, PXRD structures and DFT/TDDFT

Mohammed Enamullah[a,*], Mohammad Al-moktadir Zaman[a], Mortuza Mamun Bindu[a], Dennis Woschko[b], Mohammad Khairul Islam[a], Christoph Janiak[b,*]

[a] Department of Chemistry, Jahangirnagar University, Dhaka 1342, Bangladesh
[b] Institut für Anorganische Chemie and Strukturchemie, Universität Düsseldorf, Düsseldorf D-40204, Germany

ARTICLE INFO

*Article history:*
Received 14 February 2021
Revised 25 March 2021
Accepted 2 April 2021
Available online 13 April 2021

*Keywords:*
Mn(II)-(*R* or *S*)-(Ar)-salicylaldimine
*Chiroptical* properties and ECD spectra
Chirality induction at-metal and diastereoselection
PXRD-structure
DFT/TDDFT

ABSTRACT

Pseudotetrahedral high-spin *bis*[(*S or R*)-N-1-(Ar)ethyl-salicylaldiminato-$\kappa^2$N,O]-Λ/Δ-Mn(II) {Ar = $C_6H_5$ (Mn*S*L1 or Mn*R*L1), *p*-$MeOC_6H_4$ (Mn*S*L2 or Mn*R*L2) and *p*-$BrC_6H_4$ (Mn*S*L3 or Mn*R*L3)} are synthesized from reactions between enantiopure Schiff base ligands (*S* or *R*)-N-1-(Ar)ethyl-salicylaldimine and manganese(II) chloride with induction of Λ/Δ-chirality-at-metal. ESI mass spectra show the parent ion peak for the mononuclear species at *m/z* 504 (Mn*R*L1 or Mn*S*L1) and 662 (Mn*S*L3 or Mn*R*L3). The molar conductance values imply mononuclear and non-electrolyte nature of the complexes with metal-to-ligand 1:2 stoichiometry in dimethylformamide (DMF). Electronic circular dichroism (ECD) spectra exhibit mirror-image relationships, and hence confirm enantiopurity or enantiomeric excess of the *R*- or *S*-ligated complexes in solution. It suggests the diastereomer or diastereomeric excess of Δ-Mn*R*L or Λ-Mn*S*L in solution combined with the analyses on experimental and simulated ECD spectra by Density Functional Theory/Time-dependant Density Functional Theory (DFT/TDDFT), resulting from diastereoselectively induced Δ- or Λ-chiralityat-metal. In the contrast, DFT optimized structures in gas-phase disclose Λ-Mn*R*L or Δ-Mn*S*L diastereomer slightly more stable than Δ-Mn*R*L or Λ-Mn*S*L by 2–4 kcal/mol. Variable temperature magnetic moment values ($\mu_{eff.}$ = 5.25−5.55 $\mu_B$ at 263−321 K) correspond to the high-spin state of Mn(II)-complexes in methanol. Cyclic voltammograms demonstrate two one electron charge transfer processes for $Mn^{III/II}$ and $Mn^{II/I}$ couples in acetonitrile, respectively. Powder XRD patterns reveal a well-defined crystalline nature and allow structure determination for the Mn*R*L3, using the Expo-2014 program followed by Rietveld refinement. PXRD structure suggests the formation of four-coordinated mononuclear manganese(II)-complex by the two phenolate-oxygen and two imine-nitrogen atoms from two molecules of Schiff base ligands in a pseudotetrahedral geometry.



## 1. Introduction

Bidentate N^O-chelate Schiff base ligands coordinate to the transition metal ions and provide four coordinated non-planar $C_2$-symmetrical metal complexes with tetrahedral or pseudotetrahedral to square-planar geometry [1]. The molecular structures of metal-*chiral*-Schiff base complexes are of continued interests in the context of *chiroptical* properties, Λ/Δ-chirality induction at-metal and diastereoselectivity [2]. The enantiopure *R*- or *S*-Schiff base ligands (*R* or *S*-N^O) upon coordination to the metal ion induce chirality-at-metal with right (Δ)- and left (Λ)-handedness and provide two diastereomers of Δ-M(*R*-N,O)$_2$ and Λ-M(*R*-N,O)$_2$ {or Λ-M(*S*-N,O)$_2$ and Δ-M(*S*-N,O)$_2$} [3-14]. The ratio of the two diastereomers is phase dependant, that is, can be different in the liquid, solid or gas phases. The noncovalent inter- and/or intramolecular interactions at solid-state and solute-solvent interactions in solution result in a free energy difference between the two diastereomers and hence lead to formation of one diastereomer thermodynamically favored (*i.e.*, as major diastereomer). Indeed, ligand chirality and substituents, steric constraints brought by the ligand, metal ions and counter anions selection, solute-solvent interactions, pH of solution, redox reactions and crystallization protocol can considerably influence the phenomenon [3-15]. Solid-state

* Corresponding authors.
*E-mail addresses:* enamullah@juniv.edu (M. Enamullah), janiak@uni-duesseldorf.de (C. Janiak).

https://doi.org/10.1016/j.molstruc.2021.130455
0022-2860/

*versus* solution studies show a solvation-induced helicity inversion at-metal centre from Λ- to Δ-diastereomer and *vice versa* [3a,15].

Our recent works on transition metal-complexes with chiral N^O-chelate Schiff base ligands [16], structural analyses, Δ/Λ-chirality induction at-metal and diastereoselection exhibit preferred formation of Δ-M or Λ-M diastereomer in tetrahedral or pseudotetrahedral *bis*[(*R or S*)-N-1-(Ar)ethyl-salicylaldiminato-/-oxo-naphthaldiminato-$\kappa^2$N,O]-Δ/Λ-M(II) (*M* = Fe, Co, Ni, Cu, Zn) [3-12]. The phenomenon was studied in details using X-ray and PXRD analyses, spectroscopy ($^1$H NMR-/ECD-/VCD), thermal analyses (DSC) and computational procedure (DFT/TDDFT), respectively. The most reliable method, in this connection, is X-ray structure determination which assigns the absolute configuration of the metal ion at solid-state. The structure determination indicates that coordination of *R*- or S-ligands to the metal ions, in generally, provides Λ-M-*R* or Δ-M-*S* as major diastereomer in an enantiopure single crystals [3-12,15]. Indeed, in a few cases, both diastereomers coexist in an enantiopure single crystal [2h,5]. However, studies in solution reveal existence of a dynamic diastereomeric-equilibrium between the two diastereomers, which can lead Λ/Δ-helicity inversion to one direction as a function of variable time and/or temperature, as evidenced by $^1$H NMR and ECD spectra [3-8].

Manganese complexes with Schiff base ligands show considerable interests mainly in the context of variable coordination geometries and oxidation states, catalytic activities, and antiferromagnetic behaviors [17-19]. Indeed, no report has yet been available on mononuclear non-planar Mn(II)-complexes with chiral Schiff base ligands, (*S* or *R*)-(Ar)ethyl-salicylaldimine. In view of further investigations on Λ/Δ-chirality induction at-metal and diastereoselection, we have synthesized the mononuclear pseudotetrahedral *bis*[(*S or R*)-N-1-(Ar)ethyl-salicylaldiminato-$\kappa^2$N,O]-Λ/Δ-Mn(II), and characterized them by elemental analysis, IR-, UV–Vis.-, ECD- and mass-spectroscopy, redox potential, paramagnetism and thermal analyses (DSC), respectively. The optimized structures and excited state properties by DFT/TDDFT are employed to rationalise the experimental results. Combined studies on experimental and computational results are considered to gain further insight into *chiroptical* properties, and hence to explain Λ/Δ-chirality induction at-metal and diastereoselection phenomenon in *R*- or *S*-ligated complexes. Finally, PXRD measurements are carried out to elucidate the molecular structures of the complexes.

## 2. Experimental

### 2.1. Materials and measurements

Vibrational (IR) spectra were recorded on a Nicolet iS10 spectrometer (KBr discs) at ambient temperature. Absorption (UV–Vis.) spectra were recorded on a Shimadzu UV 1800 spectrophotometer in methanol at 25 °C. The molar conductance was measured with the Mettler Toledo Fivego (Model F3) conductivity metre in dimethylformamide (DMF) at 25 °C. ECD spectra were obtained with a JASCO Spectropolarimeter (J715) in methanol at 25 °C. Elemental analyses were run on a Vario EL instrument from Elementaranalysensysteme. ESI mass spectra were recorded with a Thermo-Finnigan TSQ 700. Cyclic voltammetry (CV) experiments were carried out with an Epsilon$^{TM}$ Instruments (BASi) electrochemical analyser using tetra-N–butyl–ammonium-hexafluorophosphate (TBAP) as supporting electrolyte in acetonitrile at 25 °C. The three-electrode measurements were employed with (i) a platinum disc working electrode, (ii) a platinum wire auxiliary electrode and (iii) a Ag/AgCl reference electrode. The solution containing the sample Mn*S*L2 and TBAP was deoxygenated with nitrogen gas for 10 min prior to use. Differential Scanning Calorimetery (DSC) analyses were performed on the Shimadzu DSC-60 in a range from 30 to 300 °C (just before the decomposition temperature) under nitrogen atmosphere at a rate of 10 K min$^{-1}$. Syntheses of the enantiopure Schiff bases (*S* or *R*)-N-1-(Ar)ethyl-salicylaldimine {Ar = $C_6H_5$ (*S*-HL1 or *R*-HL1), *p*-$OCH_3C_6H_4$ (*S*-HL2 or *R*-HL2) and *p*-$BrC_6H_4$ (*S*-HL3 or *R*-HL3)} were reported in our previous literature [16].

### 2.2. Syntheses of the complexes

Two equivalents of enantiopure Schiff base (*R* or *S*)-N-1-($C_6H_5$)ethyl-salicylaldimine (*R*-HL1 or *S*-HL1) (450.4 mg, 2.0 mmol) were dissolved in 10 mL of methanol and stirred for 10 min. One equivalent of $MnCl_2{\cdot}4H_2O$ (198.0 mg, 1.0 mmol) was dissolved in 5 mL of methanol. This salt solution was poured into the Schiff base solution and stirred under nitrogen atmosphere at room temperature. The colour changed from light-yellow to green after *ca*. 20 h of stirring. The volume of the solvent from the mixture solution was reduced to *ca.* 50% in *vacuo* at 30 °C until precipitate appeared and left standing this solution until complete precipitation. After 12 h, the solution was filtered and the deep-green precipitate collected. The precipitate was washed with n-pentane (2 mL) for three times and dried in *vacuo* at 30 °C followed by nitrogen gas to obtain deep-green microcrystals of *bis*[(*R or* S)-N-1-($C_6H_5$)ethyl-salicylaldiminato-/-oxo-$\kappa^2$N,O]-Mn(II) (Mn*R*L1 or Mn*S*L1). The same procedure was followed to synthesise the *bis*{(*R* or S)-N-1-(Ar)ethyl-salicylaldiminato-$\kappa^2$N,O]-Mn(II) (Mn*R*L2 or Mn*S*L2 and Mn*R*L3 or Mn*S*L3) using the Schiff bases (*R* or *S*)-N-1-(Ar)ethyl-salicylaldimine {Ar = *p*-$MeOC_6H_4$ (*R*-HL2 or *S*-HL2) and *p*-$BrC_6H_4$ (*R*-HL3 or *S*-HL3)}, respectively. Several attempts were made to grow single crystals suitable for X-ray structure determination, unfortunately none of them were succeeded. Analytical data including elemental analysis, IR, ESI-mass and molar conductance values are listed into Supplementary Information.

### 2.3. Paramagnetic measurements

$^1$H NMR spectra were run on a Bruker AC 300 Spectrometer operating at 400 MHz in $CDCl_3$ at 25 °C. For variable temperature (VT) paramagnetic measurements, $^1$H NMR spectra for Mn*S*L2 in methanol were recorded at different temperatures starting from *ca.* 321 K cooling down to *ca.* 263 K and again heating up to *ca.* 321 K, respectively. The values of magnetic susceptibility ($\chi$/M) and moment ($\mu_{eff}/\mu$B) were measured based on the Evans' method [20], following our previous literatures [7,12,21]. An internal capillary tube containing acetone-$d_6$ in TMS (*ca.* 5% v/v) was used as an external standard and instrument lock. Dioxane in methanol (*ca.* 0.5%, v/v) was used as an internal reference compound to measure the paramagnetic shift with respect to TMS peak in complex solution (or in methanol). Concentration changes of complex solution with temperature were corrected by considering solvent's density changes [22a]. The methanol peaks (C*H*$_3$ and O*H*) were used for temperature calibration (to find actual temperature) in solution [22b].

### 2.4. Powder X-ray diffraction (PXRD)

PXRD data for the Schiff base (*R*-HL3) and deep green microcrystals of Mn*S*L3 and Mn*R*L3 were collected on a Bruker D2 phaser diffractometer using a flat sample holder (low background sample holder) with Cu-K$\alpha$ radiation ($\lambda$ = 1.54182 Å) in a continuous scan mode within the range of 5–50° (2$\theta$) at ambient temperature. PXRD structure for Mn*R*L3 was solved using the Expo-2014 program [23]. The background of the powder diffraction pattern was modelled by a shifted Chebyshev function. The pattern was indexed using the first 27 most intense peaks (at 5–50 °) with the program DICVOL06 [24], resulting in a triclinic symmetry for the complex. Calculated density consideration suggests that there

is only one molecule of the complex in the unit cell. Analysis of the powder pattern by the FINDSPACE module of the EXPO2014 reveals that the complex crystallises in either the non-chiral space group *P*1 or the chiral space group *P*1. As the present complex contains *chiral*-ligands and induced chirality at-metal centre, structure solution was carried out considering the space group *P*1. For structure solution, we used DFT optimized structures (log files) for both the Δ- and Λ-diastereomers as input structures. The solution was carried out by global optimization of structural models using simulated annealing technique. The metal atom was selected as the centre of rotation and anti-bump restraints were assigned to the C, N and O atoms during structure solution. Amongst the 10 trial structures, the best one was chosen based on the minimum cost function value, and used as the initial structural model for the Rietveld refinement [25-27]. Standard restraints were applied only to the phenyl rings during the refinement process [26,28]. Hydrogen atoms bonded to carbon atoms were placed at calculated positions automatically. The summary of crystal data and structure refinement parameters is listed in Table 1.

**Table 1**
Summary of crystal data and structures refinement parameters.

| Compound Mole formula | Δ-Mn*R*L3 $C_{30}H_{26}Br_2MnN_2O_2$ | Λ-Mn*R*L3 $C_{30}H_{26}Br_2MnN_2O_2$ |
|---|---|---|
| Formula weight | 661.3 | |
| Temperature (K) | 298 | |
| Crystal system | triclinic | |
| Wavelength (Å) | 1.54056 | |
| Space group | *P*1 | |
| a (Å) | 6.244 | 6.249 |
| b (Å) | 9.160 | 9.161 |
| c (Å) | 15.134 | 15.140 |
| $\alpha$ (°) | 92.707 | 92.715 |
| $\beta$ (°) | 96.352 | 96.397 |
| $\gamma$ (°) | 101.727 | 101.709 |
| Volume (Å$^3$) | 840.082 | 841.198 |
| Z | 1 | |
| $2\theta$ interval (°) | 5.0 – 50.4 | |
| Scan speed (Deg./min) | 1.5129 | |
| Acquisition time (min) | 30 | |
| No. of counts | 830 | |
| No. of reflections | 300 | |
| No. of background points | 8 | |
| $R_p$ | 4.895 | 5.797 |
| $R_{wp}/R_{exp}$ | 6.702/2.482 | 7.644/2.505 |
| $\chi^2$ | 7.291 | 9.309 |
| Goodness-of-fit | 2.700 | 3.051 |

### 2.5. Computational method

The optimized structures and excited state properties by DFT/TDDFT were performed using Gaussian 09 [29]. The gas-phase initial geometries for the diastereomers Λ-Mn*R*L1, Λ-Mn*R*L2, Λ-Mn*R*L3, Δ-Mn*S*L2 and Δ-Mn*S*L3 were generated from the X-ray structures for corresponding homoleptic Λ-Co*R*L1, Λ-Co*R*L2, Λ-Co*R*L3, Δ-Co*S*L2 and Δ-Co*S*L3, respectively [4-8,12,15]. In addition, the initial geometries with opposite configured Δ-Mn*R*L1, Δ-Mn*R*L2, Δ-Mn*R*L3, Λ-Mn*S*L2 and Λ-Mn*S*L3 were created by mirror inversion of Λ-Mn*R*L1, Λ-Mn*R*L2, Λ-Mn*R*L3, Δ-Mn*S*L2 and Δ-Mn*S*L3, respectively, followed by manual inversion of the *chiral*-carbon centres [4-8,12,15]. The structures at their high-spin state (*i.e.*, $S = 5/2$, $m = 6$) were optimized with different combinations of the functionals (*e.g.*, B3LYP, M06 and BVP86) and the basis sets (*e.g.*, 6–31G(d), DEF2SVP and TZVP), respectively (Figs. S2, S4) [17d-g,19a]. The structures were further also optimized with the B3LYP functional and the mixed basis sets (*e.g.*, LANL2DZ or 6–31G(d) for CHNO and 6–31G(d) or TZVP for Mn), respectively (Fig. S3).

The excited state properties by TDDFT were performed for the diastereomeric pairs Λ-Mn*R*L2/Δ-Mn*R*L2 and Δ-Mn*S*L2/Λ-Mn*S*L2 at B3LYP/DEF2SVP//B3LYP/6–31G(d), respectively. The PCM (polarization continuum model) was incorporated using methanol as solvent and 72 excited states (roots) were considered for calculations (Table S1). Assignments on excited state properties and molecular orbitals (MOs) calculations were carried out at the same level of theory. TDDFT were further run on the Λ-Mn*S*L2 (optimized at B3LYP/6–31G(d)), using different combinations of the functionals and the basis sets, respectively, to check the reliability and validity of the methods employed. UV–Vis. and ECD spectra were generated using the SpecDis program [30] assuming Gaussian band shape with exponential half-width $\sigma = 0.33$ eV.

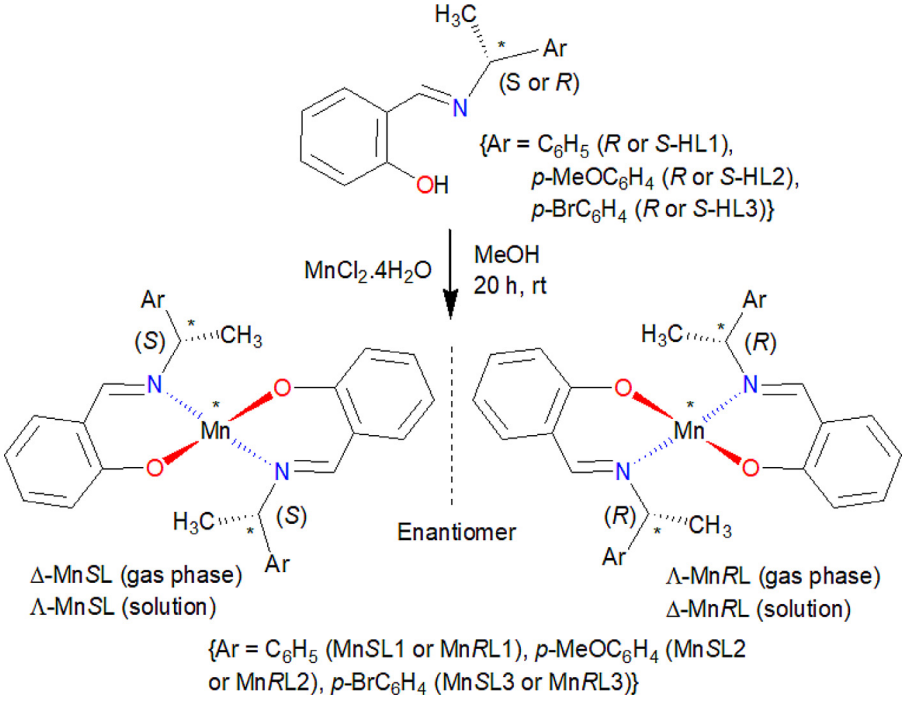


**Scheme 1.** Syntheses of *bis*[(*S or R*)-N-1-(Ar)ethyl-salicylaldiminato-$\kappa^2$N,O]-Λ/Δ-Mn(II) complexes.

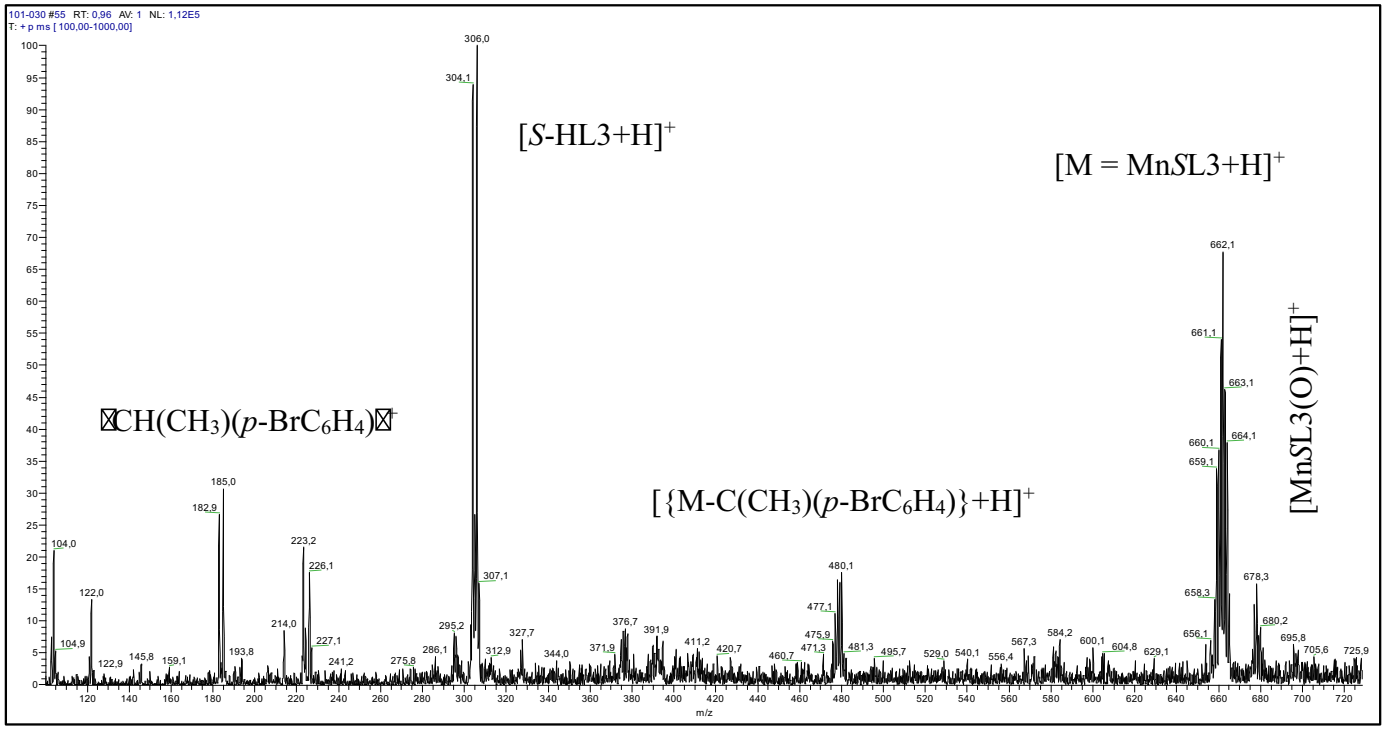


**Fig. 1.** ESI-MS spectra for Mn*S*L3.

## 3. Results and discussion

The enantiopure Schiff bases (*S* or *R*)-N-1-(Ar)ethyl-salicylaldimine (*S* or *R*-HL) coordinate to the manganese(II) chloride to provide *bis*[(*S or R*)-N-1-(Ar)ethyl-salicylaldiminato-$\kappa^2$N,O]-Λ/Δ-manganese(II) {Ar = $C_6H_5$ (Mn*S*L1 or Mn*R*L1), *p*-$MeOC_6H_4$ (Mn*S*L2 or Mn*R*L2) and *p*-$BrC_6H_4$ (Mn*S*L3 or Mn*R*L3)}, respectively (Scheme 1). IR spectra show a characteristic band at 1617−1604 $cm^{-1}$ for νC=N [4-8,12,15]. The low molar conductance values ($\Lambda_m$ = 5.75−7.50 S $cm^2$ $mol^{-1}$) suggest non-electrolyte nature of the complexes with metal-to-ligand 1:2 stoichiometry in DMF.

### 3.1. Mass spectra

ESI-MS spectra show the parent ion peak for the complexes at *m/z* 504 for $[MnRL1+H]^+$ and 662 for $[MnSL3 \text{ or } MnRL3+H]^+$ (Fig. 1, S1). The spectra are further dominated by several ions peaks at *m/z* 480 for $[\{M\text{-}C(CH_3)(p\text{-}BrC_6H_4)\}+H]^+$, 304 for [*S* or *R*-HL3+*H*]$^+$ and 183 for $[CH(CH_3)(p\text{-}BrC_6H_4)]^+$. The complexes are very sensitive to air, and readily form the oxidative adducts as shown by the ion peaks at *m/z* 520 for $[MnRL1(O)+H]^+$ and 678 for [Mn*S*L3(O) or *R*L3(O)+*H*]$^+$.

### 3.2. UV–Vis. and ECD spectra

UV–Vis. spectra for the enantiomeric pair Mn*R*L2 and Mn*S*L2, measured in methanol at 25 °C (Fig. 2), are identical and feature several bands including: (i) a very strong band below *ca.* 300 nm with absorption maxima ($\lambda_{max}$) at 256 nm ($\varepsilon_{max}$ = 18,126 l $mol^{-1}$ $cm^{-1}$) for the intra-ligand $\pi \rightarrow \pi^*$ transitions, (ii) a strong band at 300−350 nm ($\lambda_{max}$ = 315 nm, $\varepsilon_{max}$ = 5586 l $mol^{-1}$ $cm^{-1}$) for the intra-ligand n→$\pi^*$ transitions and (iii) a medium broad band at 350−460 nm ($\lambda_{max}$ = 390 nm, $\varepsilon_{max}$ = 1794 l $mol^{-1}$ $cm^{-1}$) for the metal-ligand/ligand-metal (ML/LM) charge transfer transitions. The spectra further show a very weak broad band at 500−750 nm ($\lambda_{max}$ = 630 nm, $\varepsilon_{max}$ = 135 l $mol^{-1}$ $cm^{-1}$) due to superpositions of several metal-centred d-d transitions (MM) for Mn(II)-core electrons (Fig. 2, inset) [3a,5-7,11-12,31].

The electronic circular dichroism (ECD) spectra for the enantiomeric pairs Mn*R*L1/Mn*S*L1 and Mn*R*L2/Mn*S*L2 show consistent similarities in methanol at 25 °C (Fig. 3). The spectra show several bands with opposite Cotton effects, corresponding to different electronic transtions due to $\pi \rightarrow \pi^*$/n→$\pi^*$, ML/LM and MM, as found in UV–Vis. spectra. Indeed, the spectra show expected mirror-image relationships with almost equal and opposite ellipticity maxima ($\Delta\varepsilon_{max}$) values for each enantiomeric pair in solution. Hence, ECD spectral analyses strongly support the enantiopurity or enantiomeric excess of the *R* or *S*-ligated complexes in solution [3-9,12,15,31]. The spectral data for the enantiomeric pair

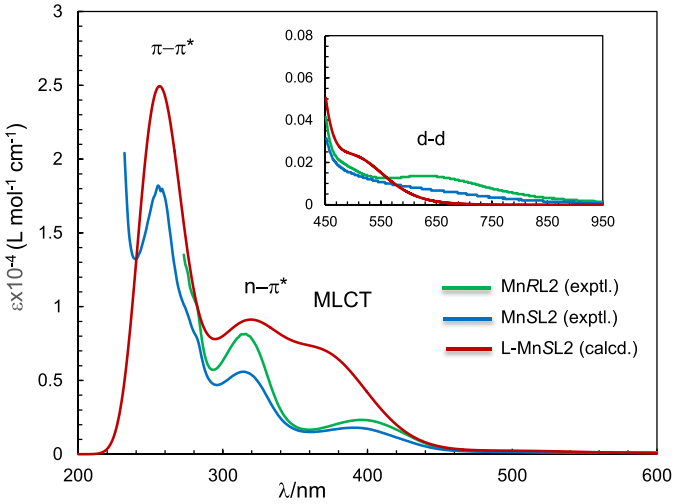


**Fig. 2.** UV–Vis. spectra for Mn*S*L2 (0.60 mM) and Mn*R*L2 (0.88 mM) in methanol at 25 °C (ε values are increased by 2 times). Simulated spectrum for Λ-Mn*S*L2 at B3LYP/DEF2SVP//B3LYP/6–31G(d) with PCM in methanol, Gaussian band shape with exponential half-width σ = 0.33 eV.

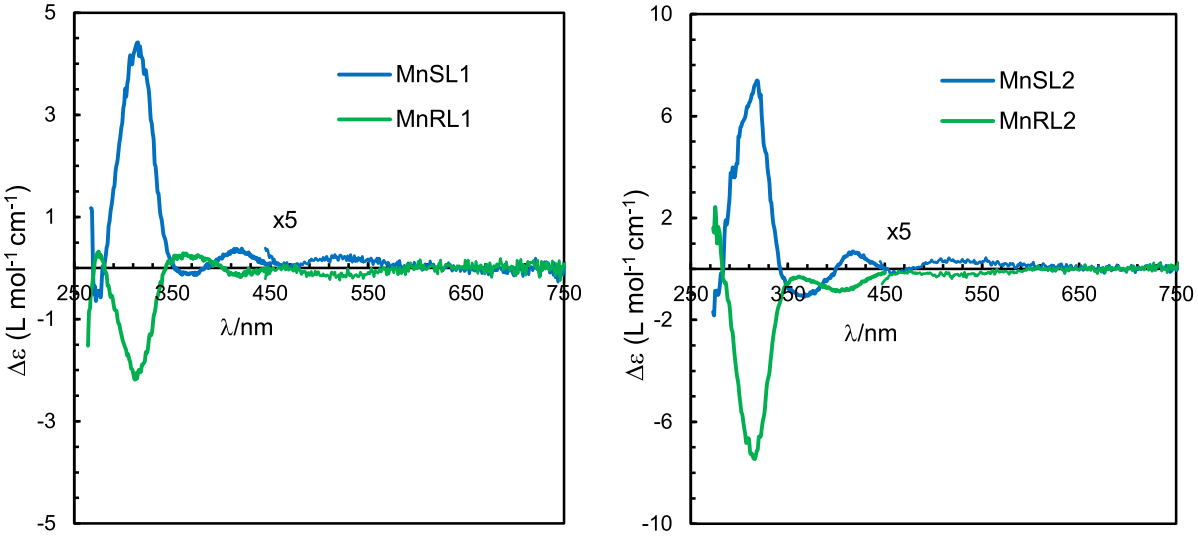


**Fig. 3.** ECD spectra for the enantiomeric pairs Mn*R*L1/Mn*S*L1 (17.74/18.86 mM at 450–750 nm; 3.54/4.77 mM at 250–450 nm) and Mn*R*L2/Mn*S*L2 (16.20/17.50 mM at 450–750 nm; 4.24/4.42 mM at 250–450 nm) in methanol at 25 °C (cell path-length: 1.0 mm).

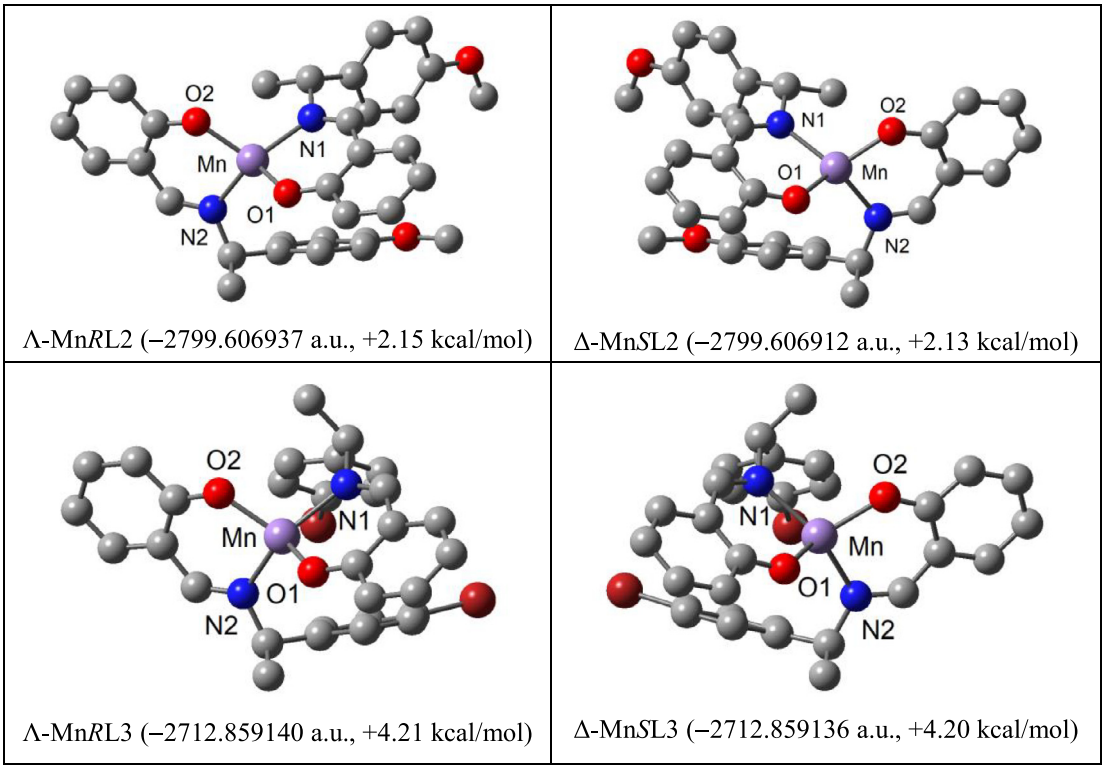


**Fig. 4.** DFT optimized structures for diastereomeric pairs Λ-Mn*R*L2/Δ-Mn*S*L2 and Λ-Mn*R*L3/Δ-Mn*S*L3 at B3LYP/6–31G(d) (hydrogen atoms are omitted for clarity).

Mn*R*L1/Mn*S*L1 demonstrate the following bands with absorption maxima at (sign and strength): *ca.* 520 nm (−/+, weak), 420 nm (−/+, weak), 370 nm (+/−, weak) and 312 nm (−/+, strong). Similarly, Mn*R*L2/Mn*S*L2 show the following bands with absorption maxima at (sign and strength): *ca.* 520 nm (−/+, weak), 424 nm (−/+, weak), 365 nm (+/−, weak) and 316 nm (−/+, strong).

### 3.3. Optimized structures

Optimized structures by DFT at B3LYP/6–31G(d) for diastereomeric pairs Λ-Mn*R*L1/Δ-Mn*R*L1, Λ-Mn*R*L2/Δ-Mn*R*L2, Λ-Mn*S*L2/Δ-Mn*S*L2, Λ-Mn*R*L3/Δ-Mn*R*L3 and Λ-Mn*S*L3/Δ-Mn*S*L3 show Λ- or Δ-diastereomers for *R*- or *S*-ligated complexes are relatively more stable by 2.13−4.21 kcal/mol (Figs. 4, S2). Similarly, optimized structures for diastereomeric pair Λ-Mn*S*L2/Δ-Mn*S*L2 with the B3LYP functional and the mixed basis sets (*e.g.*, Mn: 6–31G(d), CHNO: LANL2DZ or Mn: TZVP, CHNO: 6–31G(d)), respectively show Δ-Mn*S*L2 is relatively more stable by 1.90 or 1.73 kcal/mol (Fig. S3). Further, optimizations of Λ-Mn*R*L2/Δ-Mn*R*L2 with different combinations of the functionals (*e.g.* B3LYP, M06 and BVP86) and the basis sets (*e.g.* 6–31G(d), DEF2SVP and TZVP), respectively also reveal Λ-Mn*R*L2 as the most stable one by 1.97−5.87 kcal/mol in all methods (Fig. S4). These results are in parallel to the optimized structures for the homoleptic Co/Fe(II)-complexes which also provide relatively more stable Λ- or Δ-diastereomers for *R*- or *S*-ligated complexes [7,12]. However, some

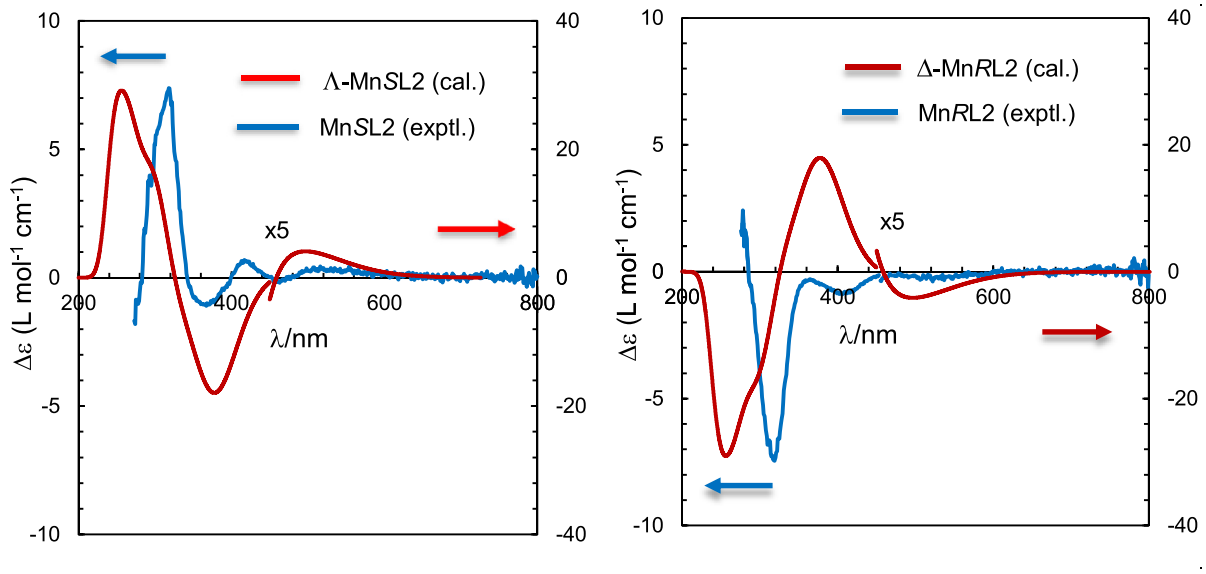


**Fig. 5.** Experimental and simulated ECD spectra for Mn*R*L2 and Mn*S*L2 in methanol at 25 °C. Mn*R*L2/Mn*S*L2 (16.20/17.50 mM at 450–750 nm and 4.24/4.42 mM at 250–450 nm). Calculated spectra for Δ-Mn*R*L2 and Λ-Mn*S*L2 at B3LYP/DEF2SVP//B3LYP/6–31G(d) with PCM in methanol.

selected bond lengths (Å) and angles (°) in relatively more stable diastereomers, for example Λ-Mn*R*L2 and Λ-Mn*R*L3, are listed in Table 3, which are comparable to the solid state X-ray data in the homoleptic Λ-Co*R*L3 [7], Δ-Cu*R*L3 [3a] and Λ-Zn*R*L3 [3b].

### 3.4. *Excited state properties and* Δ vs. Λ *configurations*

The excited state properties by TDDFT were calculated for the diastereomeric pairs Λ-Mn*R*L2/Δ-Mn*R*L2 and Λ-Mn*S*L2/Δ-Mn*S*L2 at B3LYP/DEF2SVP//B3LYP/6–31G(d), respectively. The calculated UV–Vis. spectra for each diastereomeric pair are essentially identical (Fig. S5) and fit well to the experimental spectra (Fig. 2). The calculated ECD spectra show expected mirror-image relationships with opposite Cotton effects for each diastereomeric pair (Fig. S6). The excited state properties for Λ-Mn*S*L2, calculated at different combinations of the functionals and the basis sets, respectively, provide similar UV–Vis. and ECD spectra with slightly shifted band maxima (Fig. S7), which also fit well to the experimental spectra. These results strongly endorse the reliability and validity of the methods employed in determining the excited state properties and optimization methods.

Indeed, ECD spectra mainly represent the overall nature of the *chiral* metal-complexes in solution and, in particular, are used to determine the absolute configuration of the metal centre (*i.e.*, Λ *vs.* Δ) by the observed d-d transitions bands in the vissible region [3-9,12,15]. Thus, it has successfully been used to ascertain the absolute configuration of the metal centre combined with the studies on experimental and simulated ECD spectra, resulting from chirality induction and diastereoselection by the *S*- or *R*-HL ligands in the complexes. Comparisons of experimental spectra for Mn*R*L2 and Mn*S*L2 with simulated spectra for diastereomeric pairs Λ-Mn*R*L2/Δ-Mn*R*L2 and Δ-Mn*S*L2/Λ-Mn*S*L2 reveal that the spectra for Mn*R*L2 and Mn*S*L2 fit well to those for the Δ-Mn*R*L2 and Λ-Mn*S*L2, respectively (Fig. 5). Further, spectra for Mn*R*L2 and Mn*S*L2 match well to those for the diastereomers Δ-Mn*S*L2 and Λ-Mn*R*L2, respectively. These results suggest that the spectra for Mn*R*L2 or Mn*S*L2 correspond to the diastereomer or diastereomeric excess of Δ-Mn*R*L2 or Λ-Mn*S*L2 (*i.e.*, major diastereomers) in solution, similar to Δ-M-*R* or Λ-M-*S* diastereomer (major) in the homoleptic Cu/Fe(II)-complexes with *R*- or *S*-HL ligands [3a,12]. In the contrast, Λ-M-*R* or Δ-M-*S* diastereomer is preferred in homoleptic Co/Zn(II)-complexes with *R*- or *S*-HL ligands in solution [3b,7]. Finally, it could be concluded, based on experimental and simulated ECD spectra and related literatures, an induced chirality at-metal (Δ *vs.* Λ) has been developed, which diastereoselectively prefers Δ-Mn*R*L or Λ-Mn*S*L in solution.

Despite the complexity and limitation of assignments of excited state properties for such open-shell manganese(II)-complexes [3a,5-7,11-12,31-32], some selected spectral data and their assignments are made based on orbital and population analyses (Table 2), very close to the experimental data. Excited state properties disclose that large numbers of HOMO to LUMO transitions including intra-ligand, metal-ligand and metal d-d electrons (Table S1) occur at a single wavelength (excited-state) (Fig. S1). Thus, the band at 376 nm (392 nm, experimental) with the highest oscillator strength 0.0525 (*f*) is comprised of mainly the transitions for

**Table 2**
Some selected and simplified assignments on absorption spectra for Λ-Mn$S_2$, calculated at B3LYP/DEF2SVP//B3LYP/6–31G(d) with PCM in methanol.[#].

| λ (nm) [a] | Oscillator strength (f) | MOs contributions (%) [b] | Assignments [c] |
|---|---|---|---|
| 510 (*ca.* 550sh) | 0.0025 | H-1→*L* + 1 (7), H→L (7) | MM, LM, LL |
| 376 (391) | 0.0525 | H-1→L (7), H→L (72) | MM, LM, LL |
| 332 (315) | 0.0465 | H-1→*L* + 1 (33), H→*L* + 1 (12) | MM, LM |
| 264 (*ca.* 275sh) | 0.1193 | H-5→L (64), H-4→L (13) | MM, LM, LL |
| 251 (255) | 0.0663 | H-5→*L* + 1 (39), H→*L* + 8 (38) | MM, LM, LL |

[#] Calculated for $\beta$-spin MOs consideration. [a] Experimental values are in parentheses
[b] *H* = HOMO and *L* = LUMO
[c] MM = d-d, LM = ligand-metal and LL = intra-ligand transitions.

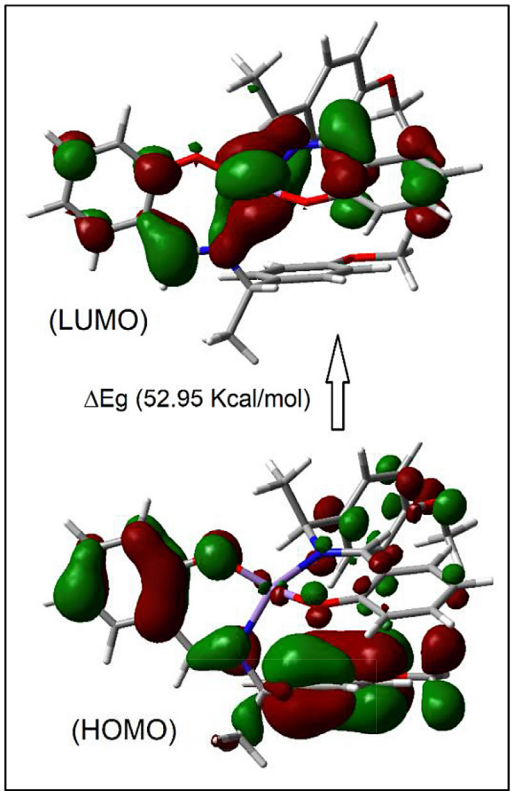


**Fig. 6.** The frontier HOMO (−0.34261 a.u.) and LUMO (−0.25823 a.u.) for Λ-Mn*SL*2, calculated at B3LYP/DEF2SVP//B3LYP/6–31G(d) for $\beta$-spin consideration.

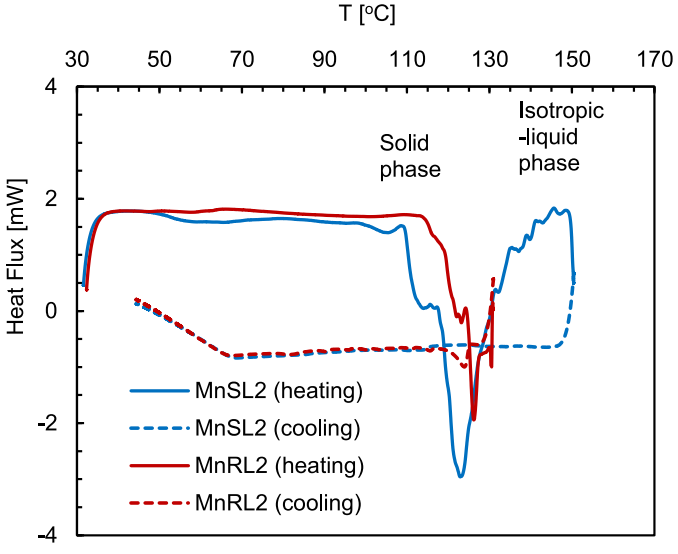


**Fig. 7.** Differential Scanning Calorimetry (DSC) curves for Mn*RL*2 and Mn*SL*2.

metal-$d_{xy}$ and salyl-/aryl-$\pi$ electrons moieties (HOMO) to metal-$d_{xy}$ and salyl-$\pi$ moieties (LUMO). The energy gap for the HOMO to LUMO (Fig. 6) transition is 52.95 kcal/mol and corresponds to the highest MOs contribution (*ca.* 72%) in the excitation protocol.

### 3.5. Solid-liquid phase transformation

The DSC heating curves for Mn*SL*2 and Mn*RL*2 show a clear phase transformation from solid to isotropic-liquid phase with exo-thermic peaks at *ca.* 123 and 126 °C and heat of transformation energies (ΔH) *ca.* −46.05 and −43.05 kJ $mol^{-1}$, respectively (Fig. 7)

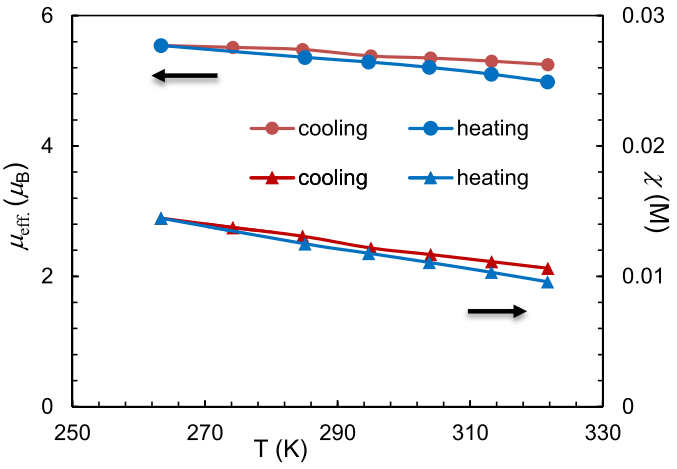


**Fig. 8.** Changes of magnetic susceptibilities ($\chi$) and moments ($\mu_{eff.}$) with temperatures for Mn*SL*2 (0.112 mM) in methanol.

[4-8,11-12]. On the other hand, the cooling curves show no corresponding peaks on the reverse direction, suggest an irreversible phase transformation for the complexes. Both the heating curves reveal a shoulder on low temperature side (by *ca.* 5–10 °C) in addition to the exo-thermic peaks, indicate the existances of both the Δ- and Λ-diastereomers in Mn*SL*2 or Mn*RL*2 at solid-state [4].

### 3.6. Paramagnetism

$^1$H NMR spectra of the complexes in $CDCl_3$ show shifting and peak broadening effects resulting from paramagnetic nature of the high-spin Mn(II)-core electrons [5,7,12]. The values of magnetic susceptibilities ($\chi$/M) and magnetic moments ($\mu_{eff.}/\mu$B) were measured based on Evans' method [20,21] over a temperature range of 263–321 K for Mn*SL*2 in methanol (Fig. 8). The relatively high magnetic moment values ($\mu_{eff.}$ = 5.25–5.55 $\mu_B$) correspond to the high-spin state of the complex [17,19a]. Indeed, the spin only magnetic moment value ($\mu_{cal.}$) for five unpaired electrons is 5.91 ($\mu$B) for tetrahedral/octahedral high-spin Mn(II)-complex, and the difference with the $\mu_{eff.}$ arises from contributions of the orbital angular magnetic moment [33]. However, the magnetic moment values remain almost steady with changes of temperature and show reproducibility for the heating and cooling cycles (Fig. 8), and thus confirm the integrity of the high-spin state of the complex in solution. In fact, there is no indication of spin-crossover transition between the high-spin and low-spin states at the extended temperature range (*i.e.*, 263–321 K), which would substantially drop the $\mu_{eff.}$ values with decreasing temperature. However, a very small change in magnetic moment values, and a narrow deviation between the heating and cooling cycles might result from decomposition of the complex with temperature and/or time in solution, as reported for the homoleptic tetrahedral high-spin Co/Fe(II)-complexes [7,12].

### 3.7. Cyclic voltammograms

Cyclic voltammograms for Mn*SL*2 were recorded at a potential range starting from 0 to −1.50 V, then to 1.50 V and finally, to 0 V (*vs.* Ag/AgCl) at a fixed or varying scan rates in acetonitrile at 25 °C, respectively (Fig. 9). The forward (reduction) wave shows a broad peak at *ca.* −0.75 V at a scan rate of 100 mV/s, which becomes more intense with faster scan rates, attribute to the reduction of $Mn^{III/II}$. Further, a weak broad shoulder (*ca.* −1.10 V) on the same wave becomes increasingly populated with faster scan

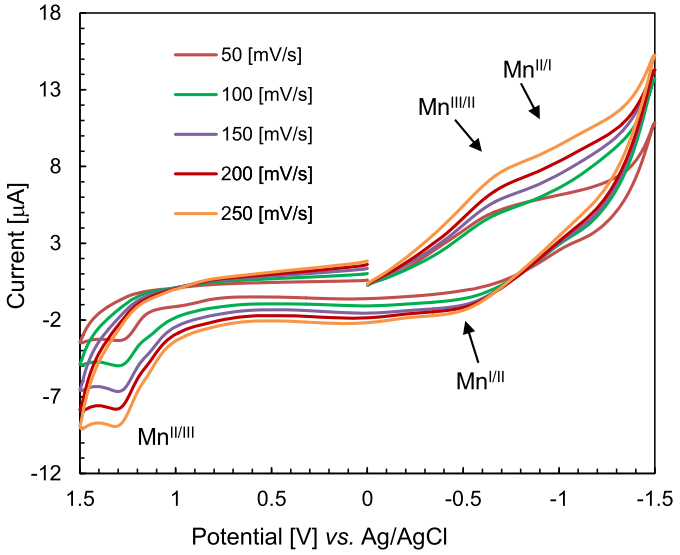


**Fig. 9.** Cyclic voltammograms for Mn*SL*2 (*ca.* 0.5 mmol dm$^{-3}$) at different scan rates; TBAP (*ca.* 0.1 mol dm$^{-3}$) in acetonitrile at 25 °C.

rates and overlaps with the decomposition peak of the electrolyte (TBAP) [6], assign for the reduction of $Mn^{II/I}$. The reverse (oxidation) wave shows a weak broad shoulder at *ca.* −0.55 V and a sharp peak *ca.* +1.30 V, which also become more intense with faster scan rates, assign for the oxidation of $Mn^{I/II}$ and $Mn^{II/III}$, respectively [17e]. The peak for $Mn^{II/I}$ or $Mn^{I/II}$ is not distinctly visible (weak intensity), due to instability of the charged species which undergo a rapid chemical transformation in solution. Indeed, the redox peak for $Mn^{IV/III}$ is usually observed at a relatively high potential (*i.e.*, < −0.40 V [18a]), which is absent in the present CV patterns. However, the homoleptic Fe*SL*2 complex shows three distinct redox peaks for three one electron charge transfer processes at *ca.* −0.38, −1.08 and −1.55 V ($E_{1/2}$), corresponds to the $Fe^{III/II}$, $Fe^{II/I}$ and $Fe^{I/0}$ couples, respectively [12]. Analyses of CV patterns at different scan rates reveal that the peak current ($i_{pc}$) increases linierly with faster scan rates (Fig. S8), a diagnostic for diffusion-controlled electrochemical process in acetonitrile [6,7,12,19f].

### 3.8. Powder XRD analysis

Powder XRD patterns for the Schiff base (*R*-HL3) and deep green microcrystals of Mn*SL*3 and Mn*RL*3 were recorded at 5 – 50° (2$\theta$) at ambient temperature (Fig. 10). The distinct PXRD patterns show the absences and/or presences of certain intense peaks in the Schiff base or complexes, indicate the coordination of the ligands to the metal(II) ion. PXRD patterns correspond to well defined crystalline nature with various degrees of crystallinity for the Schiff base and complexes [12,34,35,36]. PXRD patterns for the enantiomeric complexes Mn*SL*3 and Mn*RL*3 are essentially identical (Fig. 10), comparable to the homoleptic Fe/Co(II)-complexes [7,12]. PXRD pattern for Mn*RL*3 was used for structure determination using the Expo-2014 program [23] followed by Rietveld refinement [25-28]. It has been reported that for a given *chirality* of the ligands (*R* or *S*), only one Λ- or Δ-configured complex could be found based on the single-crystal absolute structure determination using the Flack parameter [3-9]. Our previous results and related literatures demonstrate that diastereoselection and chirality induction at-metal, in general, provide Λ-M-*R* or Δ-M-*S* as the only diastereomer (or major) in the investigated enantiopure crystal of M(II)-(*R* or *S*)-N,O-chelate Schiff base complexes [2g-h,n-o,3,5,7,9,15]. However, this does not rule out the presence of the other diastereomer Δ-M-*R* or Λ-M-*S* (minor one) in the enantiopure crystals mixture of the bulk sample. Thus, the bulk sample of Mn*RL*3 could contain either Δ-Mn*RL*3 or Λ-Mn*RL*3 diastereomer or a mixture of both (racemic mixture). For PXRD structures solution calculations, we used DFT optimized structures for both Δ-Mn*RL*3 and Λ-Mn*RL*3 as input files and found no significant differences in the crystal data and structure refinement parameters (Tables 1). Indeed, the Rietveld refinement plots exhibit good agreement amongst the experimental, calculated, difference and background PXRD profiles for both the diastereomers (Figs. 11, S9). The molecular structures determinations reveal that the two molecules of N^O-chelate Schiff base ligands form a mononuclear, pseudotetrahedral $N_2O_2$-coordination sphere around the manganese atom (Fig. 12). The

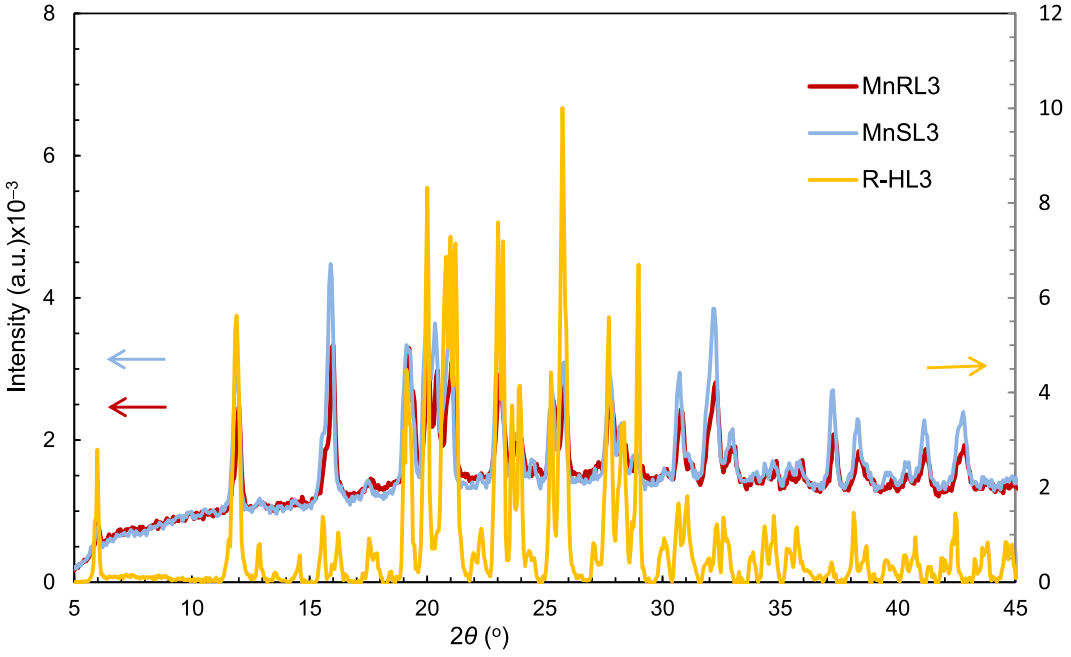


**Fig. 10.** Powder XRD patterns for the Schiff base (*R*-HL3) and enantiomeric complexes (Mn*SL*3 and Mn*RL*3) at ambient temperature.

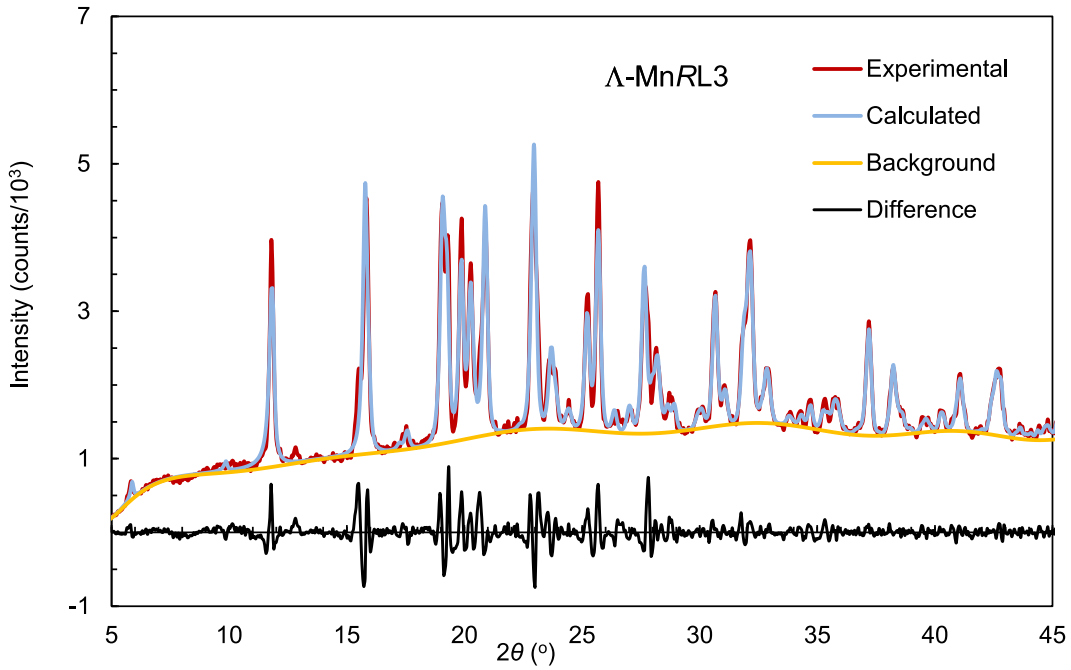


**Fig. 11.** PXRD patterns for Mn*R*L3: experimental, calculated (Λ-Mn*R*L3), difference and background profiles after Rietveld refinement.

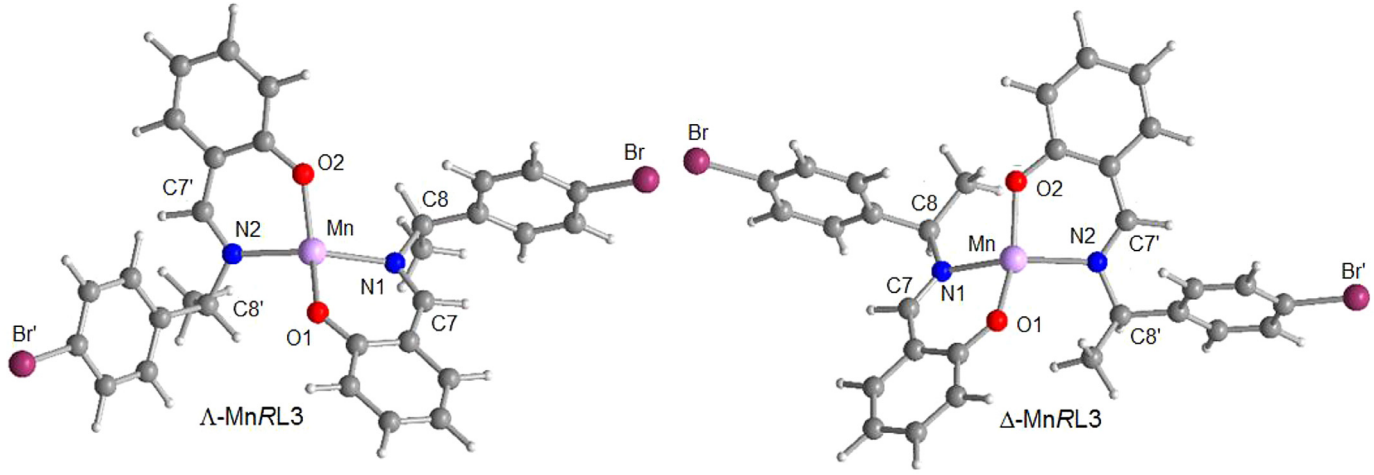


**Fig. 12.** Molecular structures for Λ-Mn*R*L3 and Δ-Mn*R*L3 from Rietveld refinement.

metal ion is four-coordinated by the two phenolate-oxygen and two imine-nitrogen atoms from two molecules of Schiff bases in pseudotetrahedral geometry. By considering a molecular (albeit not crystallographic) pseudo-$C_2$-axis passing through the centre of O1…O2 edge, metal atom and N1…N2 edge, the absolute configuration of Δ- or Λ-form is assigned (Scheme 1) and denoted as part of the complexes' description. In the space group P1, the asymmetric unit contains a full molecule. We note that the quality of the Rietveld refinements was mainly intended to confirm the pseudotetrahedral molecular geometry. We do not want to draw further reaching conclusions on the metal-centred chirality as the differences in refinement parameters for Δ-Mn*R*L3 and Λ-Mn*R*L3 as quite small, with only a slight preference for the former. Some selected bond lengths and angles are listed in Table 3, which are comparable to those reported in the crystal structures of the homoleptic M(II)-complexes ($M$ = Co [7], Cu [3a], Zn [3b]) and also comparable to the DFT optimized structures (Table 3). The metal-ligand distances reveal the Mn−O bond as shorter than Mn−N due to strong bonding interaction between the negatively charged oxygen atom ($O^-$) and positively charged Mn(II) ion. The values of the imine bond length (*i.e.*, N1-C7 or N2-C7′ = 1.28–1.30 Å) indicate the carbon-nitrogen double bond character, while the bonding angles for C7-N1-C8 or C7′-N2-C8′ (117–121°) represent $sp^2$-hybridization of the imino-nitrogen atom.

The distortion between tetrahedral and square-planar coordinated geometry around a four-coordination metal ion can be assessed on the basis of the dihedral angle ($\theta/^o$ = angle between O1−Mn−N1 and O2-Mn-N2 planes) and its normalized function ($\tau_{tet\text{-}sq} = \theta/90°$ with 1.0 being ideally tetrahedral, 0.0 ideally square-planar) from the molecular structure. We calculated $\theta$ and $\tau_{tet\text{-}sq}$ values for both Δ-Mn*R*L3 and Λ-Mn*R*L3 from PXRD and DFT structures, respectively and compared with X-ray structure values for the homoleptic Co/Cu/Zn(II)-complexes [3,7] (Table 3). The values of $\tau_{tet\text{-}sq}$ = 0.91 for Co and Zn indicate a near ideal tetrahedral coordination, $\tau_{tet\text{-}sq}$ = 0.37 for Cu a distortion from tetrahedral towards more square-planar and $\tau_{tet\text{-}sq}$ = 0.61–0.73 for Mn a distortion from intermediate situation between tetrahedral and square-planar towards tetrahedral. The results show that Λ-

**Table 3**
Selected bond lengths (Å) and angles (°) in the optimized structures and PXRD structures in comparison to the homoleptic Co [7], Cu [3a] and Zn [3b] complexes.

| Bond lengths/angles [Å/°] | DFT optimized structures | | | X-ray structures for homoleptic complexes | | | PXRD structures | |
|---|---|---|---|---|---|---|---|---|
| | Λ-Mn*RL*2 | Δ-Mn*RL*3 | Λ-Mn*RL*3 | Λ-Co*RL*3 [a] | Δ-Cu*RL*3 [b] | Λ-Zn*RL*3 [c] | Δ-Mn*RL*3 | Λ-Mn*RL*3 |
| M-O1 | 1.987 | 1.983 | 1.989 | 1.911 | 1.881 | 1.924 | 1.982 | 1.987 |
| M-O2 | 1.989 | 1.983 | 1.989 | 1.914 | 1.898 | 1.920 | 1.980 | 1.989 |
| M-N1 | 2.147 | 2.139 | 2.158 | 2.000 | 1.986 | 2.026 | 2.140 | 2.158 |
| M-N2 | 2.149 | 2.139 | 2.158 | 2.007 | 1.989 | 2.028 | 2.138 | 2.156 |
| C7-N1/C7′-N2 | 1.301 | 1.30 | 1.300 | 1.297 | 1.281 | 1.292 | 1.297 | 1.299 |
| O1–M–O2 | 125.37 | 138.83 | 129.16 | 118.18 | 159.40 | 118.08 | 138.83 | 129.14 |
| N1–M–N2 | 133.06 | 145.58 | 142.30 | 126.67 | 153.01 | 126.15 | 145.58 | 142.33 |
| N1–M–O1 | 90.95 | 90.10 | 89.55 | 95.15 | 93.21 | 94.47 | 90.10 | 89.55 |
| N2–M–O2 | 89.65 | 90.09 | 89.55 | 94.33 | 93.11 | 95.31 | 90.01 | 89.57 |
| N1–M–O2 | 111.78 | 101.91 | 106.57 | 112.20 | 92.91 | 112.85 | 101.93 | 106.56 |
| N2–M–O1 | 110.44 | 101.91 | 106.58 | 112.28 | 90.31 | 111.95 | 101.98 | 106.56 |
| C7-N1-C8 | 116.50 | 121.08 | 116.51 | 116.46 | 117.56 | 116.42 | 120.97 | 116.43 |
| C7′-N2-C8′ | 116.70 | 121.08 | 116.52 | 115.57 | 119.26 | 117.70 | 121.13 | 116.46 |
| $\theta$ [°] [d] | 74.59 | 54.67 | 65.27 | 81.98 | 33.26 | 82.31 | 54.69 | 65.27 |
| $\tau_{tet\text{-}sq}$ [e] | 0.83 | 0.61 | 0.73 | 0.91 | 0.37 | 0.91 | 0.61 | 0.73 |

[a] *Bis*[(*R*)-N-1-(*p*-Br$C_6H_4$)ethyl-salicylaldiminato-$\kappa^2$N,O]-Λ-Co(II), (Λ-Co*RL*3) [7].
[b] *Bis*[(*R*)-N-1-(*p*-Br$C_6H_4$)ethyl-salicylaldiminato-$\kappa^2$N,O]-Δ-Cu(II), (Δ-Cu*RL*3) [3a].
[c] *Bis*[(*R*)-N-1-(*p*-Br$C_6H_4$)ethyl-salicylaldiminato-$\kappa^2$N,O]-Λ-Zn(II), (Λ-Zn*RL*3) [3b].
[d] Dihydral angle ($\theta$ [°] = angle between the two planes N1–Mn–O1 and N2–Mn–O2) and [e] $\tau_{tet\text{-}sq} = \theta/90$ °.

Mn*RL*3 ($\theta$ = 65.27) tends more towards the tetrahedral by *ca.* 10° in comparison to Δ-Mn*RL*3 ($\theta$ = 54.69). At the same time, Λ-Mn*RL*3 was calculated slightly more stable than Δ-Mn*RL*3 in the gas phase (discussed above). The preferred solid-state diastereomers are Λ-Co*RL*3 [7] and Λ-Zn*RL*3 [3b] in the enantiopure crystals with Co and Zn in near tetrahedral coordination, while for more square-planar Cu, the preferred solid-state diastereomer is Δ-Cu*RL*3 [3a]. According to the $\tau_{tet\text{-}sq}$ values the distortion at Mn is in-between Co/Zn and Cu, which gives no clear indication on the preferred diastereomer in the solid-state for Mn. Unfortunately, many attempts to grow single crystals in X-ray quality were failed. It is interesting to speculate that the co-existence of Λ-Mn*RL*3 and Δ-Mn*RL*3 may prevent a high-quality crystal growth.

## Conclusions

Pseudotetrahedral high-spin *bis*[(*S or R*)-N-1-(Ar)ethyl-salicylaldiminato-$\kappa^2$N,O]-Λ/Δ-Mn(II) {Ar = $C_6H_5$ (Mn*SL*1 or Mn*RL*1), *p*-Me$OC_6H_4$ (Mn*SL*2 or Mn*RL*2) and *p*-Br$C_6H_4$ (Mn*SL*3 or Mn*RL*3)} are synthesized from enantiopure Schiff base ligands (*S* or *R*)-N-1-(Ar)ethyl-salicylaldimine with Λ/Δ-chirality induction at-metal. Conductance measurements suggest the mononuclear and non-electrolyte nature of the complexes in DMF. PXRD structure determination for Mn*RL*3 indicates that the two phenolate-oxygen and two imine-nitrogen atoms from two molecules of the Schiff base ligands coordinate to the manganese(II) in a pseudotetrahedral geometry. ECD spectra with mirror-image relationships ascertain the enantiopurity or enantiomeric excess of *R*- or *S*-ligated complexes in solution. The results suggest Δ/Λ-chirality induction at-metal combined with the studies on experimental and simulated ECD spectra, which diastereoselectively provides Δ-Mn*RL* or Λ-Mn*SL* diastereomer in solution. Variable temperature magnetic measurements suggest the high-spin state of Mn(II)-complexes in methanol. CV measurements demonstrate the presence of $Mn^{III/II}$ and $Mn^{II/I}$ couples in acetonitrile, correspond to two one electron charge transfer processes, respectively.

## Author statement

Mohammed Enamullah and Christoph Janiak are credited to 30% in each (total of 60%).

All other authors are credited to remaining 10% in each (total of 40%).

## Declaration of Competing Interest

None.

## Acknowledgement

We acknowledge Wazed Miah Science Research Centre (WMSRC) at Jahangirnagar University, Dhaka, Bangladesh for CV data. Our sincere thanks to Professor Walid Houry and Vaibhav Bhandari, Department of Biochemistry, Faculty of Medicine, University of Toronto, Canada, for running ECD spectra. We thank the Alexander-von-Humboldt Foundation, Bonn, Germany for funding the research of ME and CJ through the Research Group Linkage Program. We are grateful to Professor ABP Lever, Department of Chemistry, York University, Toronto and the Computecanada.ca (https://ccdb.computecanada.ca/) Ontario, Canada for using computational resources.

## Supplementary materials

Supplementary material associated with this article can be found, in the online version, at doi:10.1016/j.molstruc.2021.130455.

## References

[1] (a) P.G. Cozzi, Chem. Soc. Rev. 33 (2004) 410; (b) H. Gröger, Chem. Rev. 103 (2003) 2795; (c) K.R. Jain, W.A. Herrmann, F.E. Kühn, Coord. Chem. Rev. 252 (2008) 556; (d) M. Shibasaki, M. Kanai, S. Matsunaga, N. Kumagai, Acc. Chem. Res. 42 (2009) 1117; (e) J. Niemeyer, G. Kehr, R. Frohlich, G. Erker, Dalton Trans. (2009) 3731; (f) P. Adão, J.O.Costa Pessoa, R.T. Henriques, M.L. Kuznetsov, F. Avecilla, M.R. Maurya, U. Kumar, I. Correia, Inorg. Chem. 48 (2009) 3542; (g) Z.-.X. Xu, Z.-.T. Huang, C.-.F. Chen, Tetrahedron Lett 50 (2009) 5430; (h) Z. Chu, W. Huang, L. Wang, S. Gou, Polyhedron 27 (2008) 1079; (i) D. Koth, M. Gottschaldt, H. Görls, K. Pohle, Beilstein J. Org. Chem. 2 (2006) 17; (j) C.T. Cohen, T. Chu, G.W. Coates, J. Am. Chem. Soc. 127 (2005) 10869; (k) X. Zhou, J. Zhao, A.M. Santos, F.E. Kuehn, Z. Naturforsch. B: Chem. Sci. 59 (2004) 1223; (l) G. Santoni, D. Rehder, J. Inorg. Biochem. 98 (2004) 758; (m) J.F. Larrow, E.N. Jacobsen, Top. Organomet. Chem. 6 (2004) 123.
[2] (a) A.von Zelewsky, in: Stereochemistry of Coordination Compounds, John Wiley & Sons, Chichester, 1996. p. 69; (b) H. Amouri, M. Gruselle, in: Chirality in Transition Metal Chemistry: Molecules, Supramolecular Assemblies and Materials, John Wiley & Sons, Chichester, 2008, p. 40; (c) E.C. Constable, Chem. Soc. Rev. 42 (2013) 1637; (d) K.A. Jensen, Inorg. Chem. 9 (1970) 1; (e) U. Knof, A.von Zelewsky, Angew. Chem., Int. Ed. 38 (1999) 302; (f) O. Mamula, A.von Zelewsky, T. Bark, H. Stoeckli-Evans, A. Neels, G. Bernardinelli, Chem. Eur. J. 6 (2000) 3575; (g) C. Evans, D. Luneau, J. Chem. Soc. Dalton Trans. (2002) 83; (h) G. Brewer, C. Brewer, R.J. Butcher, G.T. Robichaux, C. Viragh, Inorg. Chim. Acta 410 (2014) 171; (i) E.C. Constable, G. Zhang, C.E. Housecroft, M. Neuburger, J.A. Zampese, Chem. Commun. (2010) 3077; (j) H. Sakiyama, H. Okawa, N. Matsumoto, S. Kida, Bull. Chem. Soc. Jpn. 64 (1991) 2644; (k)

H. Sakiyama, H. Okawa, N. Matsumoto, S. Kida, J. Chem. Soc. Dalton Trans. (1990) 2935; (l) Z. Dezhahang, M.R. Poopari, J. Cheramy, Y.J. Xu, Inorg. Chem. 54 (2015) 4539; (m) H. Ōkawa, M. Nakamura, S. Kida, Inorg. Chim. Acta 120 (1986) 185; (n) T. Akitsu, Y. Einaga, Polyhedron 24 (2005) 2933. *ibid*, 24 (2005) 1869; (o) T. Akitsu, Y. Einaga, Acta Crystallogr. C. 60 (2004) m640.

[3] (a) A.-C. Chamayou, G. Makhloufi, L.A. Nafie, C. Janiak, S. Lüdeke, Inorg. Chem. 54 (2015) 2193; (b) A.-C. Chamayou, S. Lüdeke, V. Brecht, T.B. Freedman, L.A. Nafie, C. Janiak, Inorg. Chem. 50 (2011) 11363.

[4] M. Enamullah, G. Makhloufi, R. Ahmed, B. Alif Joy, M.A. Islam, D. Padula, H. Hunter, G. Pescitelli, C. Janiak, Inorg. Chem. 55 (2016) 6449.

[5] M. Enamullah, A.K.M. Royhan Uddin, G. Pescitelli, R. Berardozzi, G. Makhloufi, V. Vasylyeva, A.-.C. Chamayou, C. Janiak, Dalton Trans. 43 (2014) 3313.

[6] M. Enamullah, M.A. Quddus, M.R. Hasan, G. Pescitelli, R. Berardozzi, G. Makhloufi, V. Vasylyeva, C. Janiak, Dalton Trans. 45 (2016) 667.

[7] G. Pescitelli, S. Lüdeke, A.-.C. Chamayou, M. Marolt, V. Justus, M. Górecki, L. Arrico, L. Di Bari, M.A. Islam, I. Gruber, M. Enamullah, C. Janiak, Inorg. Chem. 57 (2018) 13397.

[8] M. Enamullah, V. Vasylyeva, C. Janiak, Inorg. Chim. Acta 408 (2013) 109.

[9] M. Enamullah, M.A. Quddus, M.R. Hasan, G. Pescitelli, R. Berardozzi, G.J. Reiß, C. Janiak, Eur. J. Inorg. Chem. (2015) 2758.

[10] M. Enamullah, V. Vasylyeva, M.A. Quddus, M.K. Islam, S.-.P. Höfert, C. Janiak, CrystEngComm. 20 (33) (2018) 4724.

[11] (a) M. Enamullah, M.A. Quddus, M.M. Rahman, T.E. Burrow, J. Mol. Struct. 1130 (2017) 765; (b) M. Enamullah, M.A. Islam, B.A. Joy, B. Dittrich, G.J. Reiß, C. Janiak, Inorg. Chim. Acta 482 (2018) 935.

[12] M. Enamullah, K.S. Banu, M.A. Hossain, Ü. Kökçam-Demir, J. Mol. Struct. 1199 (2020) 126947.

[13] (a) C. Merten, R. McDonald, Y. Xu, Inorg. Chem. 53 (2014) 3177; (b) M. Albrecht, E. Isaak, M. Baumert, V. Gossen, G. Raabe, R. Fröhlich, Angew. Chem., Int. Ed. 50 (2011) 2850; (c) C.M. Álvarez, R. Carrillo, R. García-Rodríguez, D. Miguel, Chem. Commun. 47 (2011) 12765.

[14] (a) J. Gregoliński, M. Hikita, T. Sakamoto, H. Sugimoto, H. Tsukube, H. Miyake, Inorg. Chem. 55 (2016) 633; (b) S. Zahn, J.W. Canary, Science 288 (2000) 1404.

[15] N. Kordestani, H.A. Rudbaria, G. Bruno, S. Rosario, J.D. Braun, D.E. Herbert, O. Blacque, I. Correia, M.Al-M. Zaman, M.M. Bindu, C. Janiak, M. Enamullah, Dalton Trans. 49 (2020) 8247.

[16] (a) M. Enamullah, A.K.M.Royhan Uddin, A-Ch. Chamayou, C. Janiak, Z. Naturforsch. 62b (2007) 807; (b) M. Enamullah, A.K.M.Royhan Uddin, G. Hogarth, C. Janiak, Inorg. Chim. Acta 387 (2012) 173.

[17] (a) H. Temel, H. Hosgoren, Trans. Met. Chem. 27 (2002) 609; (b) K. Mitra, S. Biswas, S.K. Chattopadhyay, B. Adhikary, C.R. Lucas, Trans. Met. Chem. 30 (2005) 185; (c) P. Pandey, S. Tripathi, M. Shanmugam, R.J. Butcher, S.S. Sunkari, Inorg. Chim. Acta 495 (2019) 118997; (d) J. Adhikary, A. Chakraborty, S. Dasgupta, S.K. Chattopadhyay, R. Kruszynski, A. Trzesowska-Kruszynska, S. Stepanović, M. Gruden-Pavlović, M. Swart, D. Das, Dalton Trans. 45 (2016) 12409; (e) S. Banerjee, P. Ghorai, P. Sarkar, A. Panjac, A. Saha, Inorg. Chim. Acta 499 (2020) 119176; (f) S. Sengupta, B.N. Mongal, S. Das, T.K. Panda, T.K. Mandal, M. Fleck, S.K. Chattopadhyay, S. Naskar, J. Coord. Chem. 71 (2018) 1214; (g) B.A. Malik, J.M. Mir, J. Coord. Chem. 71 (2018) 104.

[18] (a) C.P. Pradeep, P.S. Zacharias, S.K. Das, Inorg. Chem. Commun. 11 (2008) 89; (b) M. Maneiro, M.R. Bermejo, M.I. Fernandez, E. Gomez-Forneas, A.M. Gonzalez-Noyaa, A.M. Tyryshkin, New J. Chem. 27 (2003) 727; (c) E. Gallo, E. Solari, C. Floriani, A. Chiesi-Villa, C. Rizzoli, Inorg. Chem. 36 (1997) 2178; (d) M.R. Bermejo, A. Castiiieiras, J.C. Garcia-Monteagudo, M. Rey, A. Sousa, M. Watkinson, C.A. McAuliffe, R.G. Pritchard, R.L. Beddoes, J. Chem. Soc., Dalton Trans. (1996) 2935; (e) A. Dutta, S. Biswas, M. Dolai, B.K. Shaw, A. Mondal, S.K. Saha, M. Ali, RSC Adv. 5 (2015) 23855.

[19] (a) L.H. Abdel-Rahman, N.M. Ismail, M. Ismael, A.M. Abu-Dief, E.A.-H. Ahmed, J. Mol. Struct. 1134 (2017) 851; (b) A.A.M. Belal, I.M. El-Deen, N.Y. Farid, Rosan Zakaria, Moamen S. Refat, Spectrochim. Acta Part A Mol. Biomol. Spectrosc. 149 (2015) 771; (c) G.S. Girolami, T.B. Rauchfuss, R.J. Angelici, in: Synthesis, Technique in Inorganic Chemistry, 3rd ed., University Science Books, Sausalito, 1999, p. 254; (d) S. Mandal, R. Saha, B. Mahanti, M. Fleck, D. Bandyopadhyay, Inorg. Chim. Acta 387 (2012) 1; (e) S. Chahmana, S. Keraghel, F. Benghanem, R. Ruíz-Rosas, A. Ourari, E. Morallón, Int. J. Electrochem. Sci. 13 (2018) 175.

[20] D.F. Evans, J. Chem. Soc. (1959) 2003.

[21] (a) W. Linert, M. Enamullah, V. Gutmann, R.F. Jameson, Monat. Chem. 125 (1994) 661; (b) M. Enamullah, W. Linert, J. Coord. Chem. 35 (1995) 325; (c) M. Enamullah, J. Coord. Chem. 42 (1997) 231.

[22] (a) R.F. Brunel, K.V. Bibber, in: International Critical Table, Mac Graw-Hill, N.Y., 1926, p. 27; (b) D.S. Raiford, C.L. Fisk, E.D. Becker, Anal. Chem. 51 (1979) 2050.

[23] A. Altomare, C. Cuocci, C. Giacovazzo, A. Moliterni, R. Rizzi, N. Corriero, A. Falcicchio, J. Appl. Cryst. 46 (2013) 1231.

[24] A. Boultif, D. Louer, J. Appl. Cryst. 37 (2004) 724.

[25] H. Rietveld, Acta Crystallogr. 22 (1967) 151.

[26] (a) T. Dey, P. Chatterjee, A. Bhattacharya, S. Pal, A.K Mukherjee, Cryst. Growth Des. 16 (2016) 1442; (b) S. Mondal, M. Mukherjee, K. Dhara, S. Ghosh, J. Ratha, P. Banerjee, A.K. Mukherjee, Cryst. Growth Des. 7 (2007) 1716.

[27] R. Rahmani, A. Djafria, A. Chouaiha, A. Djafric, F. Hamzaouia, R. Rizzid, A. Altomare, J. Mol. Struct. 1143 (2017) 259.

[28] E.W. Abigail, K. Maruyoshi, C.E. Hughes, P.B. Steven, D.M.K. Harris, Cryst. Growth Des. 16 (2016) 1798.

[29] Gaussian 09, Revision D.01, M.J. Frisch, G.W. Trucks, H.B. Schlegel, G.E. Scuseria, M.A. Robb, J.R. Cheeseman, G. Scalmani, V. Barone, B. Mennucci, G.A. Petersson, H. Nakatsuji, M. Caricato, X. Li, H.P. Hratchian, A.F. Izmaylov, J. Bloino, G. Zheng, J.L. Sonnenberg, M. Hada, M. Ehara, K. Toyota, R. Fukuda, J. Hasegawa, M. Ishida, T. Nakajima, Y. Honda, O. Kitao, H. Nakai, T. Vreven, J.A. Montgomery, Jr., J.E. Peralta, F. Ogliaro, M. Bearpark, J.J. Heyd, E. Brothers, K.N. Kudin, V.N. Staroverov, R. Kobayashi, J. Normand, K. Raghavachari, A. Rendell, J.C. Burant, S.S. Iyengar, J. Tomasi, M. Cossi, N. Rega, J.M. Millam, M. Klene, J.E. Knox, J.B. Cross, V. Bakken, C. Adamo, J. Jaramillo, R. Gomperts, R.E. Stratmann, O. Yazyev, A.J. Austin, R. Cammi, C. Pomelli, J.W. Ochterski, R.L. Martin, K. Morokuma, V.G. Zakrzewski, G.A. Voth, P. Salvador, J.J. Dannenberg, S. Dapprich, A.D. Daniels, Ö. Farkas, J.B. Foresman, J.V. Ortiz, J. Cioslowski, D.J. Fox, Gaussian, Inc., Wallingford CT (2009).

[30] T. Bruhn, A. Schaumlöffel, Y. Hemberger, G. Bringmann, 25 (2013) 243.

[31] M. Enamullah, M.A. Hossain, M.M. Bindu, M.K. Islam, M. Al-M. Zaman, J. coord. Chem. 73 (2020) 1745.

[32] A. Ipatov, F. Cordova, L.J. Doriol, M.E. Casida, J. Mol. Struct. (THEOCHEM) 914 (2009) 60.

[33] A.F. Orchard, Magnetochemistry, Oxford University Press, Oxford, 2003.

[34] M. Enamullah, B.A. Joy, M.K. Islam, J. Mol. Struct. 1175 (2019) 56.

[35] (a) S.R. Annapure, A.S. Munde, S.D Rathod, Der Chem. Sinica 7 (2016) 47; (b) T. Dey, P. Chatterjee, A. Bhattacharya, S. Pal, A.K. Mukherjee, Cryst. Growth Des. 16 (2016) 1442; (c) S. Karki, L. Fabian, T. Friscic, W. Jones, Org. Lett. 9 (2007) 3133 16.

[36] (a) N. Kavitha, P.V.A. Lakshmi, J. Saudi Chem. Soc. 21 (2017) S457; (b) C.-Y. Chen, P.-Y. Cheng, H.-H. Wu, H.-M. Lee, Inorg. Chem. 46 (2007) 5691; (c) K.M. Parida, M. Sahoo, S. Singha, J. Mol. Catalysis A: Chemical 329 (2010) 7.